AGU PUBLICATIONS

Geochemistry, Geophysics, Geosystems

Key Points:
- The software calculates melt migration pathways and crustal thickness at mid-ocean ridges
- The software can process three-dimensional mantle flow models of segmented mid-ocean ridges

Supporting Information:
- Supporting Information S1
- Data Set S1

Correspondence to:
H. Bai,
baigo@umd.edu

MeltMigrator: A MATLAB-based software for modeling three-dimensional melt migration and crustal thickness variations at mid-ocean ridges following a rules-based approach

Hailong Bai[1] (ID)**, Laurent G. J. Montési[1]** (ID)**, and Mark D. Behn[2]** (ID)

[1]Department of Geology, University of Maryland, College Park, Maryland, USA, [2]Department of Geology and Geophysics, Woods Hole Oceanographic Institution, Woods Hole, Massachusetts, USA

Abstract MeltMigrator is a MATLAB®-based melt migration software developed to process three-dimensional mantle temperature and velocity data from user-supplied numerical models of mid-ocean ridges, calculate melt production and melt migration trajectories in the mantle, estimate melt flux along plate boundaries, and predict crustal thickness distribution on the seafloor. MeltMigrator is also capable of calculating compositional evolution depending on the choice of petrologic melting model. Programmed in modules, MeltMigrator is highly customizable and can be expanded to a wide range of applications. We have applied it to complex mid-ocean ridge model settings, including transform faults, oblique segments, ridge migration, asymmetrical spreading, background mantle flow, and ridge-plume interaction. In this technical report, we include an example application to a segmented mid-ocean ridge. MeltMigrator is available as a supplement to this paper, and it is also available from GitHub and the University of Maryland Geodynamics Group website.

1. Introduction

The majority of basaltic oceanic crust is formed along mid-ocean ridges, which, in the context of plate tectonics, represent a type of divergent plate boundaries [e.g., *Hess*, 1962]. As adjacent tectonic plates move apart, the underlying hot mantle rises and melts. These melts are then transported and collect beneath the ridge axis, where they are extracted, cool, and accrete to form new oceanic crust.

The oceanic crustal thickness has been inferred from seismic reflection [e.g., *Carbotte et al.*, 2008] and refraction data [e.g., *Le Pichon et al.*, 1965], gravity measurement [e.g., *Kuo and Forsyth*, 1988; *Lin et al.*, 1990], ophiolite observations [e.g., *Nicolas et al.*, 1996], basalt geochemistry [e.g., *Klein and Langmuir*, 1987], and numerical models [e.g., *Reid and Jackson*, 1981]. The oceanic crust has an average thickness of 6–7 km thick [*White et al.*, 2001], but varies locally as a function of spreading rate [e.g., *Lin and Phipps Morgan*, 1992] and in more complex geological settings such as near transform faults and fracture zones [e.g., *Gregg et al.*, 2007], overlapping spreading centers [e.g., *Canales et al.*, 2003], oblique segments [e.g., *Montési et al.*, 2011], ultraslow spreading centers [*Dick et al.*, 2003], migrating ridges [e.g., *Carbotte et al.*, 2004], and plume-ridge interaction zones [e.g., *White*, 1997]. MeltMigrator makes it possible to investigate the effects of melt migration on these crustal thickness variations.

Melting takes place in a broad region (>100 km) in the mantle beneath mid-ocean ridges [e.g., *MELT Seismic Team*, 1998; *Evans et al.*, 1999; *Key et al.*, 2013]; however, crustal accretion is confined to a narrow region, <2 km from the ridge axis [*Macdonald*, 1982]. This contrast indicates that melt must be focused from the wide generation region toward the ridge axis. Several mechanisms have been proposed to explain melt focusing, including dynamic pressure gradients in the mantle [*Spiegelman and McKenzie*, 1987], stress-induced melt bands [*Katz et al.*, 2006], hydrofracturing [*Sleep*, 1988], reactive infiltration instability [*Kelemen et al.*, 1995], and permeability barriers associated with a crystallization front [*Sparks and Parmentier*, 1991].

Here we describe a software that simulates the effect of focusing along a permeability barrier, as proposed by *Sparks and Parmentier* [1991]. The permeability barrier forms at the base of thermal boundary layer, where rapid crystallization of plagioclase and pyroxene clogs the pore space and prevents further upward

migration of melts [*Kelemen and Aharonov*, 1998; *Hebert and Montési*, 2010]. A high-porosity decompaction channel is formed immediately beneath the barrier. It is then possible for melt to accumulate and travel within the decompaction channel, guided by the slope of the barrier, toward the ridge axis [*Sparks and Parmentier*, 1991].

More specifically, we follow the three-step scheme for melt focusing and extraction at mid-ocean ridges described in detail by *Montési et al.* [2011] and *Gregg et al.* [2012]. The three steps are: (1) vertical melt percolation in the asthenosphere; (2) melt collection and migration in a decompaction channel that follows a low-permeability barrier at the base of thermal boundary layer toward ridge axis; and (3) melt extraction when melt enters a damage zone associated with predefined plate boundaries. MeltMigrator calculates melt migration pathways according to these three steps, estimates melt flux along mid-ocean ridges, and predicts regional crustal thickness variations.

This software is designed to study melt migration processes occurring in the mantle. Melt storage, transport, and eruption at crustal level are ignored or idealized. We assume that a solution for the mantle flow field and temperature structure is available separately and simulate the melt production and migration in postprocessing. Thus, we do not attempt to rigorously include the effects of compaction pressure and the latent heat of fusion [*Wilson et al.*, 2014]. This simplification is useful when dealing with mid-ocean ridges with three-dimensional features such as transform faults, oblique segment, ridge migration, asymmetrical spreading, background mantle flow, and ridge-plume interaction where a more rigorous approach may be prohibitively expensive from a computational standpoint.

2. Code Availability

MeltMigrator is available from GitHub with the MIT License at https://github.com/montesi/MeltMigrator. Example COMSOL input models are available at our group website http://www.geology.umd.edu/~montesi/ Geodynamics/software.html#MeltMigrator. MeltMigrator and the example models are also available in supporting information to this article.

3. Methods

3.1. Prerequisite and Model Input

MeltMigrator is programmed in MATLAB®. The main script, `meltMain`, calls a number of attendant functions, most of which are defined in stand-alone scripts, to conduct various steps of the calculation. Here we describe the calculation procedure step by step. Scripts contained in MeltMigrator package are listed in supporting information Table S1 and a flowchart of the major calculation steps is included (supporting information Figure S1). The parameters that govern code behavior, including the definition of the plate boundaries under consideration, are set up in the script `setParameters`, removing the need to modify any of the attendant scripts. Each script starts with a description of its function, definition of its internal and external variables, and a list of dependencies (attending scripts).

The software starts by reading a pre-existing three-dimensional thermomechanical model of a mid-ocean ridge system. The model should be constructed in a Cartesian coordinate system, and extend to sufficient depth to include the bottom of the melting region. The temperature and velocity fields solved in the model should be exportable to MATLAB®. We typically use a model of mantle flow and thermal structure constructed using COMSOL Multiphysics® 4.3, which is transferred into MATLAB® using LiveLink™ for MATLAB®, with the `mphinterp` function. The software is also setup to use numerical model saved as a text file with x, y, z, velocity in x-direction, velocity in y-direction, velocity in z-direction, and temperature data organized in columns. To use this capacity, users need to set the parameter `Switch_UseCOMSOL` in `setParameters` to 0. In either mode, the name of the file containing the model is stored as the `ModelName` variable in `setParameters`.

Key parameters must be entered in the setParameters script independently from the external model input. They include the spreading rate and spreading direction (in relation to the x axis) of the ridge system, the limits of model domain, and the coordinates of waypoints that define the plate boundary. The code automatically determines the length and obliquity (defined as the angle between the plate motion direction

and the normal to the ridge axis) of each plate boundary segment and stores the necessary information in the structure Geometry.

MeltMigrator has been applied to a variety of plate boundaries settings, including intratransform spreading centers [*Hebert and Montési*, 2011], transform faults [*Bai and Montési*, 2015], and oblique segments [*Montési et al.*, 2011]. The ridge system in the demonstration model is spreading in x axis direction at a half-spreading rate of 2 cm/yr. The plate boundary is defined by three ridge segments offset by one transform fault and one oblique segment (Figure 1).

3.2. Melting Function and Calibration

Partial melting beneath mid-ocean ridges results from adiabatic decompression of the mantle. The degree and extent of melting is a function of temperature, pressure, bulk chemical composition, and volatile content (e.g., H_2O). To simulate mantle melting in the routine, we can use either thermodynamic models such as MELTS and pMELTS [*Ghiorso*, 1994; *Ghiorso and Sack*, 1995; *Ghiorso et al.*, 2002; *Asimow and Stolper*, 1999] or a melting parameterizations [e.g., *Reid and Jackson*, 1981; *McKenzie and Bickle*, 1988; *Hirschmann*, 2000; *Katz et al.*, 2003; *Behn and Grove*, 2015]. The latter approach is typically preferred when dealing with three-dimensional calculations due to its computational efficiency. In the MeltMigrator, the melting function is implemented as a user-defined function `meltFunction` (a function of depth z and temperature T), which can be an inline function or an external function script.

Multiple melting parameterizations have been developed through theoretical and experimental studies [e.g., *Langmuir et al.*, 1992; *Kinzler and Grove*, 1992; *Iwamori*, 1994; *Kinzler*, 1997; *Hirschmann*, 2000; *Katz et al.*, 2003; *Till et al.*, 2012; *Behn and Grove*, 2015]. In the simplest case, the equilibrium melt fraction for small degrees of melting (5–25%) is approximated as a linear function of temperature in relation to the solidus and liquidus—i.e., the difference between temperature and solidus, scaled by the difference between solidus and liquidus [*Bottinga et al.*, 1978; *Reid and Jackson*, 1981]. The linear melting formula by *Reid and Jackson* [1981], which is adopted in the demonstration example, is provided in the `meltFunctionRJ1981` script. Alternatively, the script `meltFunctionMELTS` uses a look-up table of results from the alphaMELTS thermodynamics software [*Smith and Asimow*, 2005].

It is possible to automatically adjust the melting function so that a reference crustal thickness, specified by the variable named `CrustalThickness_Reference`, is produced at a certain point along the mid-ocean ridge axis. The calibration is conducted along a two-dimensional vertical cross section, perpendicular to a selected ridge segment, ideally away from transform faults, oblique segments, and/or borders of the computational domain. In the example model, the script places the cross section at the center of the longest ridge segment. The temperature and vertical velocity data from the external model are interpolated on a grid of sampling points on the cross section from the input model result. The crustal thickness obtained by collecting all the melt produced in the selected cross section, H_a, is given by:

$$H_a = \int_0^{L_m} \int_{z_b}^0 \frac{\partial F}{\partial z} \frac{v_z}{2V_p} dz \ dx \tag{1}$$

where F is the melt fraction calculated using `meltFunction`, v_z is the vertical velocity of the mantle, V_p is the half-spreading rate, L_m is the length of the cross section, and z_b is the depth to the base of the melting column [e.g., *Reid and Jackson*, 1981]. The calculated value of H_a is then divided by the user-defined reference crustal thickness to produce a scaling factor, with which `meltFunction` is updated, so that desired level of crustal thickness can be generated along the target portion of ridge segments. This scaling factor can be interpreted as a measure of the efficiency of melt extract, or a correction on the melting function parameters. The calibration operation is optional and can be switched on/off using the variable named `Switch_MeltCalibration` in `setParameters`.

As noted above, it is also possible to use MeltMigrator with thermodynamic models in mantle melting calculation (e.g., alphaMELTS) [*Smith and Asimow*, 2005] by calling `meltFunctionMELTS` as `meltFunction` for melt fraction calculation, although this tends to be computationally expensive. alphaMELTS is a versatile program that utilizes the MELTS [*Ghiorso and Sack*, 1995] and pMELTS [*Ghiorso et al.*, 2002] algorithms to calculate the equilibrium assemblages of multicomponent systems, such as the mantle, along a user-defined thermodynamic path. It may perform batch, fractional or continuous melting, and crystallization calculations
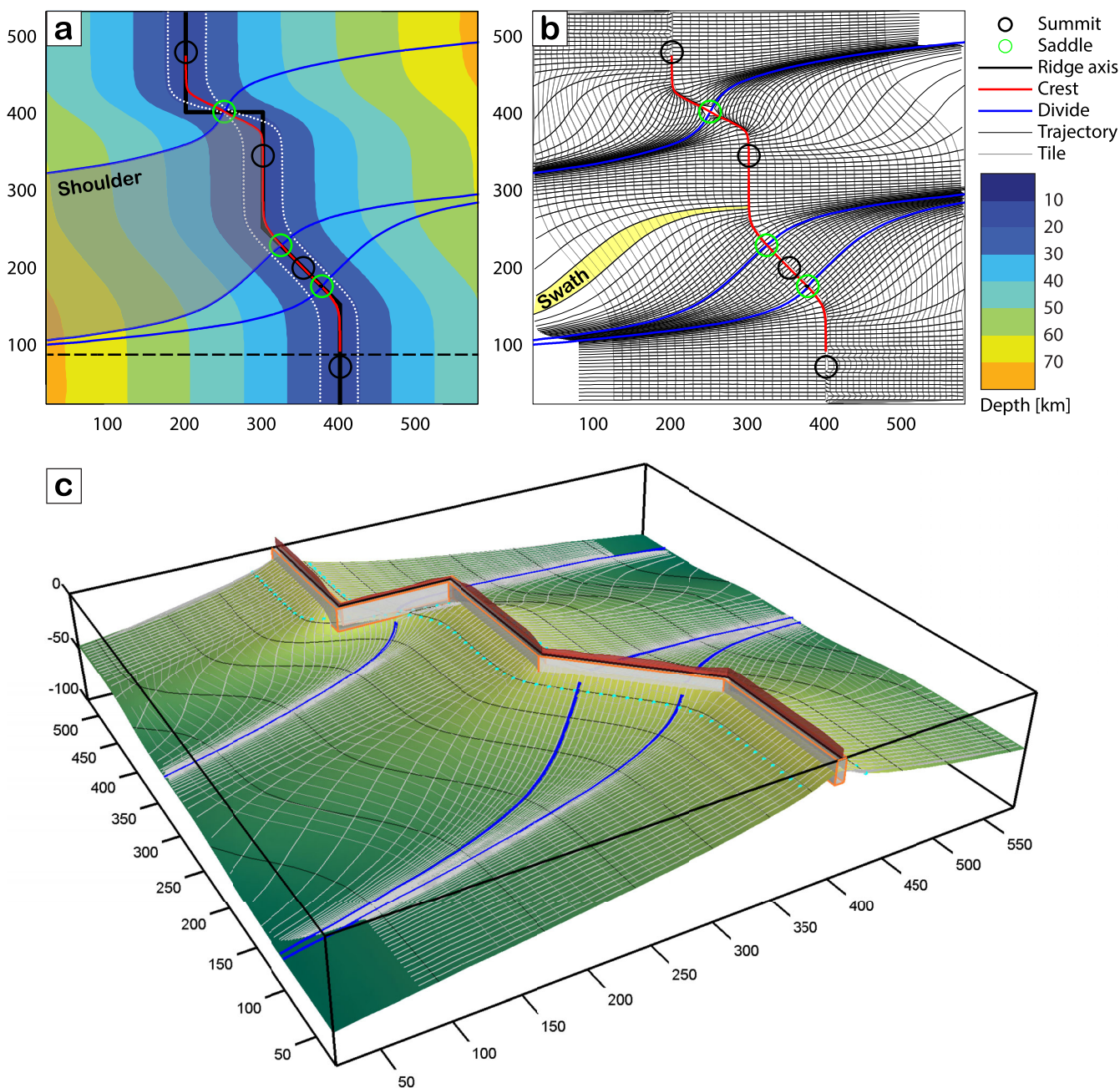
Figure 1. Permeability barrier and melt migration setup for a generic mid-ocean ridge model with three spreading segments offset by one transform fault and one oblique segment. (a) The plate boundary is indicated by the thick black line. The colors reflect the depth of the barrier. Crest, divides, summits, and saddles are displayed as shown in the legend. A shoulder is highlighted as the shaded region. The dashed line indicates the cross section used for calibrating the melt function. The white dots serve as seeds for the melt trajectories shown in Figure 1b. (b) Melt trajectories and associated tessellation of the lid. A representative swath is highlighted in yellow. (c) Three-dimensional rendition of the barrier (green surface with black depth contours), shoulder divides (blue), melt trajectories (white with cyan seed), and tiles. The orange box represents the melt extraction zone. The height of the red surface along the plate boundary is proportional to the accreted crustal thickness.

in anhydrous, water-undersaturated, or water-saturated settings. It also features a batch mode, making the large-scale automatic processing possible.

To use alphaMELTS in our calculations, we constructed a look-up table of melt fraction and temperature as a function of depth and mantle temperature. In the example provided in the supporting information, we use the isentropic mode of alphaMELTS, which assumes continuous melting with a retained melt fraction of 1%. We start with the chemical composition of depleted MORB mantle (DMM) derived by *Workman and*

Hart [2005]. For each mantle potential temperature, we increase depth until the mantle is solid and initiate isentropic decompression, recording the melt fraction and temperature at each depth. For each sampling point of the numerical model, we take the temperature and pressure into the look-up table to find the corresponding melt fraction. Besides melt fraction, alphaMELTS outputs a rich collection of results, including the major and trace element composition of the solid and the liquid, abundance and composition of mineral phases, and the physical properties of all phases present, which can also be stored in the look-up table and used to evaluate the chemical properties of the magma (the function of tracking chemical species is not included in the current version of MeltMigrator).

3.3. Permeability Barrier Sampling and Characterization

A critical aspect of the three-step melt migration procedure adopted here is the involvement of a permeability barrier at the base of thermal boundary layer [*Sparks and Parmentier*, 1991; *Montési et al.*, 2011]. The barrier forms a lid to the upward melt migration zone and will be referred interchangeably as the permeability barrier or the lid. The permeability barrier appears where the melt crystallizes rapidly [*Korenaga and Kelemen*, 1997] and is often associated with the multiple saturation point of pyroxene and plagioclase [*Kelemen and Aharonov*, 1998; *Hebert and Montési*, 2010].

The permeability barrier forms a two-dimensional surface embedded in the three-dimensional temperature field. The determination of the barrier is done by a stand-alone function `lidSample`. First, a sampling grid is overlain on the computational domain (sampling resolution information is stored in structure `Res`). A depth-sampling vector is devised with a finer sampling spacing at shallower depth, where the permeability barrier is most likely located. For each grid point, the temperature in the sampling column is obtained by interpolating the temperature data imported from the numerical model (e.g., using `mphinterp` for COMSOL Multiphysics® models or MATLAB® function `scatteredInterpolant` for models constructed with other software). The temperature at which the lid is formed is defined as the solution to a user-defined function `lidTemperature`, which is set by default to

$$T_{lid} = 1240 + 1.9z \tag{2}$$

where T_{lid} is expressed in °C and z in km, following *Montési and Behn* [2007] and *Hebert and Montési* [2010]. This equation represents approximately the locus of plagioclase/pyroxene multiple saturation during basalt crystallization [*Kelemen and Aharonov*, 1998], with the effects of pressure [*Yang et al.*, 1996] incorporated. The depth of permeability barrier in each sampling column is then solved using `lidDepth` (by default, `lidDepth` uses the MATLAB® equation solver `fzero`). The x, y, and z coordinates, the temperature at the permeability barrier, barrier slope, and the horizontal gradients of the slope are calculated and stored in the MATLAB® structure `Lid`. The `Lid` structure is then saved in .mat format and called again later by several additional routines.

3.4. Melt Trajectory Tracking and Melt Swath Discretization

Melt is assumed to travel upward along the slope of the lid until it either (1) enters a melt extraction zone or (2) the slope of the lid drops below a critical value. Details on the definition of the melt extraction zone and its relation to the critical slope are given by *Montési et al.* [2011] and *Bai and Montési* [2015].

To simulate melt transport along the lid, we discretize the permeability barrier into contiguous swaths separated by melt transport lines that follow the local direction of maximum slope [*Magde and Sparks*, 1997]. Melt cannot cross these lines and all the melt produced beneath a given swath collects within a restricted portion of the melt extraction zone. To define these swaths more easily, we first analyze the morphology of the lid and define coherent regions, or shoulders, where the melt would collect at a single point if there were no melt extraction zone.

The permeability barrier is a curved surface (Figure 1), which by analogy to land topography can be described in terms of summits and depressions. Summits are connected by crests that roughly follow mid-ocean ridge segments and separate mantle domains corresponding to the two divergent plates at the mid-ocean ridge axis [*Montési et al.*, 2011]. Each local elevation minimum along the crest defines a saddle. Starting at each saddle, divides are formed by tracking lines of maximum downhill slope along the lid. The boundary of each shoulder is set by the divides and the portion of the crest between two saddles (Figure

1a). All the melt generated underneath the shoulder would collect at the associated summit if left to propagate without limit along the lid.

The function `saddlePreparation` is used to locate saddles, crests, and divides. The user should specify the coordinate of target points near each saddle, preferentially at the center of the offset (transform fault or oblique segments). Alternatively, the user could select target points directly on the lid depth map using MATLAB® function `ginput` (use variable named `Switch_SaddleSelectionByMouse` to switch on). Because discontinuities along the mid-ocean ridge cause the isotherms to deepen, at least one saddle should be defined at each offset. In more complicated settings, more than one saddle may be needed. For example, Figure 1a shows that there are two saddles underneath the oblique segment of our demonstration model.

Saddles are defined as flat areas (0 slope) found by integrating a system of partial differential equations that describe how lid slope S_l changes with the horizontal coordinates x, y

$$\begin{cases} \dfrac{\partial x}{\partial L} = \dfrac{\dfrac{\partial S_l}{\partial x}}{\sqrt{\left(\dfrac{\partial S_l}{\partial x}\right)^2 + \left(\dfrac{\partial S_l}{\partial y}\right)^2}} \\[20pt] \dfrac{\partial y}{\partial L} = \dfrac{\dfrac{\partial S_l}{\partial y}}{\sqrt{\left(\dfrac{\partial S_l}{\partial x}\right)^2 + \left(\dfrac{\partial S_l}{\partial y}\right)^2}} \end{cases} \tag{3}$$

$$S_l = \sqrt{\left(\dfrac{\partial z_l}{\partial x}\right)^2 + \left(\dfrac{\partial z_l}{\partial y}\right)^2} \tag{4}$$

where L represents the traveled distance. We use MATLAB®'s `ode45` to solve for this system of equations.

Crests and divides are found by solving similar equations, only focused on depth z_l instead of slope

$$\begin{cases} \dfrac{\partial x}{\partial L} = \dfrac{1}{S_l}\dfrac{\partial z_l}{\partial x} \\[12pt] \dfrac{\partial y}{\partial L} = \dfrac{1}{S_l}\dfrac{\partial z_l}{\partial y} \end{cases} \tag{5}$$

To initiate the search, we first define a series of points along a circle centered at the saddle. The deepest point along that circle and the point on the circle directly opposite to it are selected as the starting point for the divides. Similarly, the highest point and the point on the opposite side of the circle are selected as the starting points for the crests. Equation (5) is then solved using MATLAB®'s `ode23`.

The resolution of saddle lines is controlled by the integration interval set by the parameter `Res.Saddle` in `setParameters`. To achieve higher accuracy, some options may be added to set up the acceptable error, either relative or absolute. Information describing the saddle points, crests, and divides are stored in structure `Saddle`.

Next, the `meltTrajectorySeed` function defines seeds from which melt trajectories are calculated. Although other strategies may be devised, we find it convenient to take equally spaced seeds along a contour of fixed temperature difference between the maximum temperature and the solidus temperature of the sampling columns (defined as `T_MeltSeed` in `setParameters`). Generally, two sets of seeds, one for each plate, are sufficient for generating melt trajectories (Figure 1a, white dots). Seeds are found from starting points identified on the two sides of the model parallel to the spreading direction by integrating a trajectory perpendicular to the temperature gradient using the `ode113` solver. Additional treatment may be needed if dealing with complex geometry.

Melt trajectories are generated using function `meltTrajectory`. First, the seeds are separated according to the shoulder that they span using a customized function `lineSegmentIntersect` [*Erdem*, 2010]. Then, trajectories are followed along directions of maximum slope upward and downward from each seed

using equation (5) and MATLAB®'s `ode23` solver. To ensure that the full trajectory is covered, a long integration time span is selected, and a fixed number of time steps is used for all the integration. This may result in repeated points at the end of the segment where the gradient is zero. The line segments are truncated to where the coordinates begin to change, by deleting the repeated points. Truncated upslope portion and downslope portions are then combined to form a complete melt trajectory line segment. The resolution of the melt trajectories is controlled by the integration interval set by the user in `setParameters`. The density of melt trajectories is controlled by the spacing of melt seeds, although additional trajectories are automatically generated if none of the seeded trajectories passes close to the saddles that form the corner of the shoulder.

Near the crests of the permeability barrier, where the slope approaches zero, numerical noise may result in unrealistic melt trajectories with abrupt turns over short distances. Some of the lines terminate before reaching the edge of the shoulder, while others extend along the crests for tens of kilometers. This pattern does not reflect the anticipated idealized behavior of the migrating melt (although mantle heterogeneities may perturb the smooth, idealized permeability barrier, and lead to irregular paths for melt migration [e.g., *Katz and Weatherley*, 2012]), but is controlled by the model discretization. This situation may be improved by adjusting the integration properties and reducing the error tolerance at the cost of prolonging the calculation process. Ultimately discretization errors are limited by the input numerical model resolution.

Melt trajectory information, including the coordinates of points on the line and the distance along the line, is stored in structure `Shoulder.Trajectory`. The depth, slope, and temperature along each melt trajectory are interpolated from the corresponding data of the permeability barrier (`Lid` structure), and saved along with the trajectory information. The melt trajectories for the example model are plotted in Figures 1b and 1c.

The portion of the lid that is defined by two adjacent melt trajectories forms a swath. Melt generated underneath a swath travels upslope along the swath and collects along a segment of the plate boundary associated with the swath. The associated plate boundary segment is identified by connecting the termination of melt trajectories to the nearest points on plate boundaries. Because our interest is in melt migration, we only consider the portion of melt trajectories beneath which melt is generated. Additionally, any portion of melt trajectories deeper than a critical depth (`LidDepthLimit`, default 60 km) is discarded, because the permeability barrier may not develop if crystallization occurs at a great depth [*Hebert and Montési*, 2010].

The function `meltSwath` assembles melt swaths and divides each swath into a predefined number of quadrilaterals. At this point, each melt trajectories may contain a different number of points and is resampled into a fixed number of points so that the quadrilaterals spanning one melt trajectory to the next conform between adjacent swaths. The areas and the center coordinates of quadrilaterals are calculated. The depth and slope of permeability barrier at the center of the quadrilateral are interpolated from the `Lid` structure. A melting column is defined from the center point at the surface of each quadrilateral down to the bottom of the model, and sampled according to a predefined depth sampling vector. At each sampling depth, the temperature and vertical velocity of the mantle are interpolated from the imported model data. Melt fraction is calculated using `meltFunction` and integrated over the entire column. We compute

$$p = \begin{cases} 0, & F < F_c \\ \max\left(v_z \dfrac{\partial F}{\partial z}, 0\right), & F \geq F_c \end{cases} \tag{6}$$

$$f = \int_{z_b}^{z_t} p \; dz \tag{7}$$

where p is the melt production rate, F_c is the critical melt fraction representing the retained melt fraction in the mantle, which is set by the parameter `MeltFractionCutoff` in `setParameters`, f is the melt flux, and z_t is the minimum depth of the melting column [*McKenzie*, 1985]. This calculation assumes that melt generated in the melting columns rises vertically, as expected from the latest estimates of mantle permeability [*Miller et al.*, 2014]. Migration along the permeability barrier is simulated by summing the melt flux in all quadrilaterals along each swath in the direction of melt migration toward the plate boundary. The swath and quadrilateral information are stored in structure `Shoulder.Swath` for later use.

3.5. Melt Extraction and Crustal Thickness Calculation

Crustal thickness calculation is conducted in the `crustCalculation` script. First, the thickness of crust accreted along the plate boundary (Figure 2a) is calculated by the `meltExtraction` function. As described in *Montési et al.* [2011], we defined a Melt Extraction Zone (MEZ) along plate boundaries and assume that all melt that enters the MEZ is extracted to the nearest plate boundary. The MEZ may be associated with structural damages such as diking and fracturing in the brittle lithosphere and the ductile shear zones at greater depth [*Nicolas*, 1986, 1990; *Kelemen et al.*, 1992; *Kelemen and Dick*, 1995; *Macdonald et al.*, 1996; *Perfit et al.*, 1996; *Hebert and Montési*, 2011; *Kaczmarek and Tommasi*, 2011; *Bai and Montési*, 2015]. We
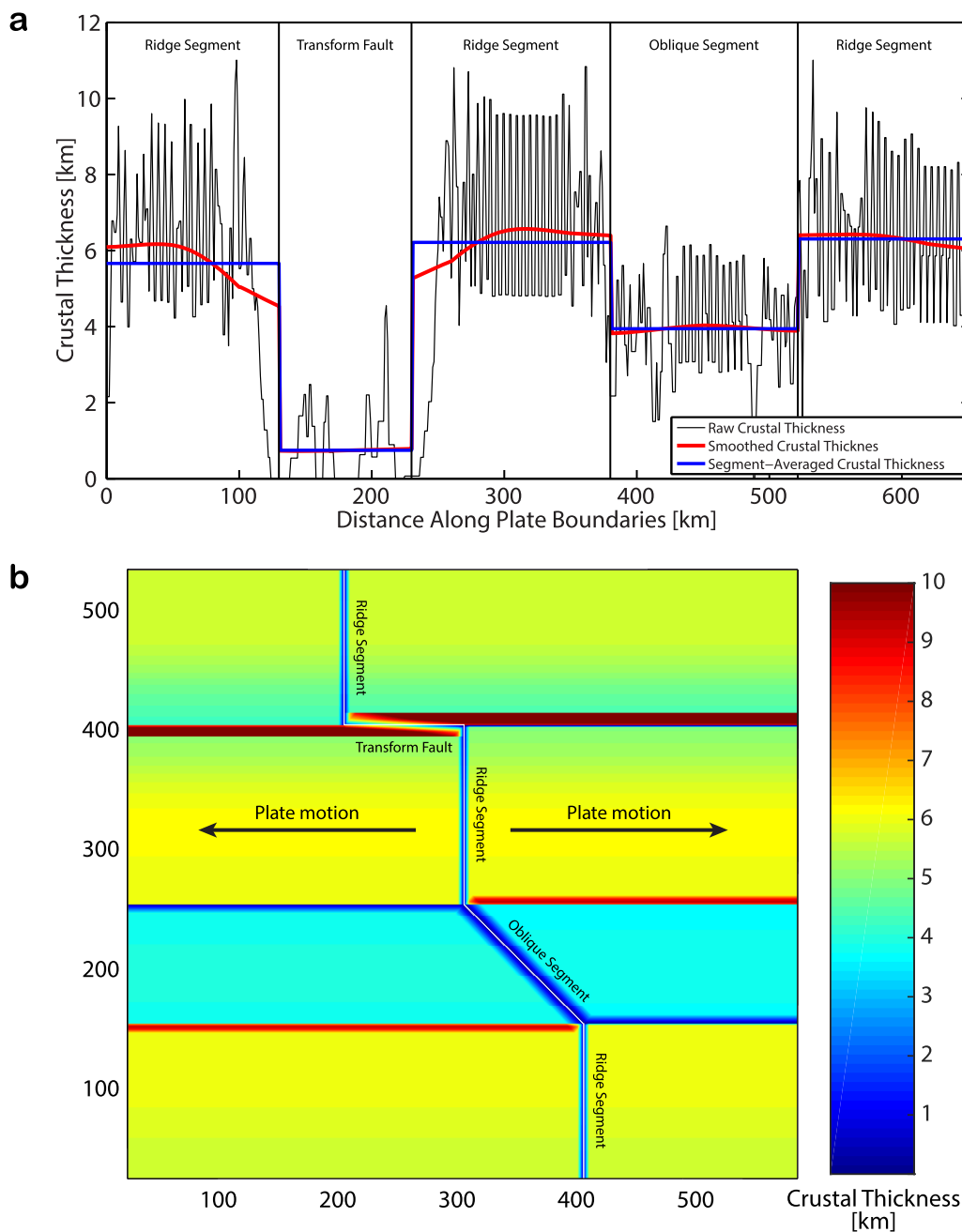

Figure 2. (a) Crustal thickness profile along plate boundary segments (labeled) for the example model. Thin black line shows unfiltered crustal thickness. The red line shows smoothed crustal thickness with a smoothing width of 60 km. The blue line shows the average crustal thickness within each plate boundary segment. (b) Map view of crustal thickness distribution over seafloor in the example model. Spreading directions and plate boundary segments are labeled.

simplify the MEZ as a box extending from the plate boundaries to an extraction width of d_e and an extraction depth of z_e (Figure 1c). Second, in the `crustalHistory` function, crustal thickness is advected following plate motion to generate a map of crustal thickness (Figure 2b) over the entire computational domain [*Bai and Montési*, 2015].

Melt extraction in the model is controlled by three parameters: s_e (`ExtractionSlope`), d_e (`ExtractionWidth`), and z_e (`ExtractionDepth`). Starting with the deepest quadrilateral in a swath, the function `extractionDetermination` determines if the current quadrilateral is located in the MEZ. If it is, the melt contained in that quadrilateral is assigned to the nearest plate boundary segment. If not, the melt moves onto next quadrilateral in the swath, but only if slope of the lid is larger than s_e. Otherwise the melt in that quadrilateral is trapped and refertilizes the ambient mantle, forming what we term cryptic crust. Following *Bai and Montési* [2015], we recommend using 4 km, 20 km, and 0.1 for `ExtractionWidth`, `ExtractionDepth`, and `ExtractionSlope`, respectively. The MEZ can be switched off by setting the value of `ExtractionWidth` to NaN, in which case melt can only get to the surface when it reaches a ridge segment.

The quadrilaterals within the MEZ are projected onto the nearest plate boundary segment. That projection spans a length L_d of the plate boundary and serves as the destination of the melt collected in that quadrilateral. We predefine points along the plate boundary and track the thickness of melt accumulated at each point. If a point is within the receiving segment of a quadrilateral, its crustal thickness increases by

$$dH = \frac{f_t A}{2 V_p L_d} \tag{8}$$

where A is the area of the quadrilateral and f_t is the total melt flux at the quadrilateral, due to melting directly below the quadrilateral and transport from deeper quadrilaterals along the swath. We also track the average and maximum melt fraction, the average melting depth, and the thickness of cryptic crust along the swath. After iterating over all the quadrilaterals and all the swaths, we obtain a profile of melt delivery, expressed as a crustal thickness, along the plate boundary (Figure 2a).

Model discretization often results in short-wavelength noise in the crustal thickness profile (Figure 2a). To reduce this numerical artifact, we smooth the profile using the function `fastSmooth`, [*O'Haver*, 2008]. It filters the data (e.g., crustal thickness, average melt fraction, etc.) in each plate boundary segment separately, with three passes of a sliding boxcar average over a smoothing width L_f (`SmoothingWidth`). The smoothing width decreases progressively close to the edges of the segment, but gets no smaller than $L_f/2$. The treatment removes short-wavelength noise but preserves larger-scale anomalies associated with the changes in plate boundary type and geometry (Figure 2a). The smoothing step can also be interpreted as representing redistribution of melt at crustal level and is therefore conducted segment by segment. The smoothing width L_f can be regarded as the distance of lateral dike propagation in the crust. A value of ∼50 km is geologically plausible [*Fialko and Rubin*, 1998].

The distribution of crustal thickness throughout the computational domain can be inferred from the crustal accretion profile along plate boundaries, assuming the newly formed crust is advected in the direction of spreading. For convenience, we reorient the plate boundaries such that the spreading direction is parallel to the x axis. After reorientation, we set up a new model boundary around the plate boundaries, leaving sufficient space to cover the original model. The new model geometry is then gridded into rectangular tiles.

Initially, the crustal thickness in each tile is set to 0. If a tile is within an accretion width d_a of a plate boundary, we add to its crustal thickness the thickness of crust accreted to the axis, scaled by the ratio between the tile width and the accretion width. The accretion width is typically different from the width of the MEZ, as the extracted (erupted) melt is mobile and may travel for some distance on the seafloor, in surface lava flows, lava tubes, or otherwise [*Chadwick and Embley*, 1994; *Sinton et al.*, 2002; *Smith and Cann*, 1999]. The width of the accretion zone can be set to different values at spreading centers and transform faults using the `AccretWidth_Ridge` and `AccretWidth_Transform` parameters. Each tile may collect melt accreted at several plate boundary segments.

Finally, starting from the tiles at the plate boundaries, the crustal thickness in each tile is carried onto the next tile in the spreading direction. A map of seafloor crustal thickness is produced as the output (Figure

2b). The script further calculates and reports the average crustal thickness within the ridge domain, the transform fault domain, the oblique segment domain, and the whole domain as diagnostics.

4. User Workflow

The user interacts with the software principally by adjusting parameters in the `setParameter` script. In principle, it is possible to specify all the required parameters and let the code run. However, it is often useful to check outputs at intermediate steps and adjust the necessary parameters.

In our experience, the following user workflow leads to the best results. First, edit `setParameter`. The user should specify the name of the pre-existing model, the geometry of the model bounding box and the plate boundary, then run `meltMain` through the cell labeled "Lid Sampling." This step extracts the lid information and produces plots of lid topography. Based on the graphical output, the user should specify the starting points for the saddle (variable `SaddleInitialPoint` in `setParameter`). If desired, adjust the remaining parameters in `setParameter`, which control the choice of melting function, the type of calibration, and the resolution of the lid tessellation and crustal thickness calculation. The user can then run `meltMain` to completion.

5. Conclusion

The MeltMigrator software processes three-dimensional mantle temperature and velocity data imported from external numerical models and returns melt migration trajectories, melt flux along plate boundaries, and crustal thickness distribution of the seafloor, with options of calculating mantle melting using thermodynamic models. It treats melt generation and migration as processes independent of mantle convection, and therefore is capable to handle three-dimensional mid-ocean ridge models with complex settings such as oblique segment, asymmetrical spreading, background mantle flow, and ridge-plume interaction, although compaction is represented only approximately. The software provides results that can be compared with gravity, seismic, and topographical data sets collected at mid-ocean ridges and may help users to gain insight into the melt migration and crustal accretion processes in their target regions.

The code is flexible and can be applied to mid-ocean ridge models constructed in various codes or software environments. Programmed in a modular manner, the routine can be easily tweaked or replaced based on users' need. With proper modification, it may be extended to other divergent systems such as rift zone and back-arc spreading center, and subsurface fluid migration in nondivergent settings.

References

Asimow, P. D., and E. M. Stolper (1999), Steady-state mantle-melt interactions in one dimension: I. Equilibrium transport and melt focusing, *J. Petrol.*, *40*, 475–494, doi:10.1093/petroj/40.3.475.

Bai, H., and L. G. J. Montési (2015), Slip-rate-dependent melt extraction at oceanic transform faults, *Geochem. Geophys. Geosyst.*, *16*, 401–419, doi:10.1002/2014GC005579.

Behn, M. D., and T. L. Grove (2015), Melting systematics in mid-ocean ridge basalts: Application of a plagioclase-spinel melting model to global variations in major element chemistry and crustal thickness, *J. Geophys. Res.*, *120*, 4863–4886, doi:10.1002/2015JB011885.

Bottinga, Y., C. J. Allegre, and R. N. Thompson (1978), Partial melting under spreading ridges [and discussion], *Philos. Trans. R. Soc. London A*, *288*, 501–525, doi:10.1098/rsta.1978.0031.

Canales, J. P., R. S. Detrick, D. R. Toomey, and W. S. Wilcock (2003), Segment-scale variations in the crustal structure of 150–300 kyr old fast spreading oceanic crust (East Pacific Rise, 8°15′N–10°5′N) from wide-angle seismic refraction profiles, *Geophys. J. Int.*, *152*, 766–794, doi:10.1046/j.1365-246X.2003.01885.x.

Carbotte, S. M., C. Small, and K. Donnelly (2004), The influence of ridge migration on the magmatic segmentation of mid-ocean ridges, *Nature*, *429*, 743–746, doi:10.1038/nature02652.

Carbotte, S. M., M. R. Nedimović, J. P. Canales, G. M. Kent, A. J. Harding, and M. Marjanović (2008), Variable crustal structure along the Juan de Fuca Ridge: Influence of on-axis hot spots and absolute plate motions, *Geochem. Geophys. Geosyst.*, *9*, Q08001, doi:10.1029/2007GC001922.

Chadwick, W. W., Jr., and R. W. Embley (1994), Lava flows from a mid-1980s submarine eruption on the Cleft segment, Juan de Fuca Ridge, *J. Geophys. Res.*, *99*, 4761–4776, doi:10.1029/93JB02041.

Dick, H. J. B., L. Lin, and H. Schouten (2003), An ultraslow-spreading class of ocean ridge, *Nature*, *426*, 405–412, doi:10.1038/nature02128.

Erdem, U. M. (2010), Fast line segment intersection, in *MATLAB Central*, MathWorks, Natick, Mass. [Available at https://www.mathworks.com/matlabcentral/fileexchange/27205-fast-line-segment-intersection.]

Evans, R. L., et al. (1999), Asymmetric electrical structure in the mantle beneath the East Pacific Rise at 17°S, *Science*, *286*, 752–756, doi:10.1126/science.286.5440.752.

Fialko, Y. A., and A. M. Rubin (1998), Thermodynamics of lateral dike propagation: Implications for crustal accretion at slow spreading mid-ocean ridges, *J. Geophys. Res.*, *103*, 2501–2514, doi:10.1029/97JB03105.

Ghiorso, M. S. (1994), Algorithms for the estimation of phase stability in heterogeneous thermodynamic systems, *Geochim. Cosmochim. Acta*, *58*, 5489–5501, doi:10.1016/0016-7037(94)90245-3.

Ghiorso, M. S., and R. O. Sack (1995), Chemical mass transfer in magmatic processes IV. A revised and internally consistent thermodynamic model for the interpolation and extrapolation of liquid-solid equilibria in magmatic systems at elevated temperatures and pressures, *Contrib. Mineral. Petrol.*, *119*, 197–212, doi:10.1007/BF00307281.

Ghiorso, M. S., M. M. Hirschmann, P. W. Reiners, and V. C. Kress (2002), The pMELTS: A revision of MELTS for improved calculation of phase relations and major element partitioning related to partial melting of the mantle to 3 GPa, *Geochem. Geophys. Geosyst.*, *3*(5), doi:10.1029/2001GC000217.

Gregg, P. M., J. Lin, M. D. Behn, and L. G. J. Montési (2007), Spreading rate dependence of gravity anomalies along oceanic transform faults, *Nature*, *448*, 183–187, doi:10.1038/nature05962.

Gregg, P. M., L. B. Hebert, L. G. J. Montési, and R. F. Katz (2012), Geodynamic models of melt generation and extraction at mid-ocean ridges, *Oceanography*, *25*, 8–88, doi:10.5670/oceanog.2012.05.

Hebert, L. B., and L. G. J. Montési (2010), Generation of permeability barriers during melt extraction at mid-ocean ridges, *Geochem. Geophys. Geosyst.*, *11*, Q12008, doi:10.1029/2010GC003270.

Hebert, L. B., and L. G. J. Montési (2011), Melt extraction pathways at segmented oceanic ridges: Application to the East Pacific Rise at the Siqueiros transform, *Geophys. Res. Lett.*, *38*, L11306, doi:10.1029/2011GL047206.

Hess, H. H. (1962), History of ocean basins, in *Petrologic Studies*, edited by E. F. Buddington, pp. 599–620, Geol. Soc. Am. Mem., Boulder, Colo.

Hirschmann, M. M. (2000), Mantle solidus: Experimental constraints and the effects of peridotite composition, *Geochem. Geophys. Geosyst.*, *1*, 1042–1026, doi:10.1029/2000GC000070.

Iwamori, H. (1994), ^{238}U-^{230}Th-^{226}Ra and ^{235}U-^{231}Pa disequilibria produced by mantle melting with porous and channel flows, *Earth Planet. Sci. Lett.*, *125*, 1–16, doi:10.1016/0012-821X(94)90203-8.

Kaczmarek, M.-A., and A. Tommasi (2011), Anatomy of an extensional shear zone in the mantle, Lanzo massif, Italy, *Geochem. Geophys. Geosyst.*, *12*, Q0AG06, doi:10.1029/2011GC003627.

Katz, R. F., and S. M. Weatherley (2012), Consequences of mantle heterogeneity for melt extraction at mid-ocean ridges, *Earth Planet. Sci. Lett.*, *335*, 226–237, doi:10.1016/j.epsl.2012.04.042.

Katz, R. F., M. Spiegelman, and C. H. Langmuir (2003), A new parameterization of hydrous mantle melting, *Geochem. Geophys. Geosyst.*, *4*(9), 1073, doi:10.1029/2002GC000433.

Katz, R. F., M. Spiegelman, and B. Holtzman (2006), The dynamics of melt and shear localization in partially molten aggregates, *Nature*, *442*, 676–679, doi:10.1038/nature05039.

Kelemen, P. B., and H. J. B. Dick (1995), Focused melt flow and localized deformation in the upper mantle: Juxtaposition of replacive dunite and ductile shear zones in the Josephine peridotite, SW Oregon, *J. Geophys. Res.*, *100*, 423–438, doi:10.1029/94JB02063.

Kelemen, P. B., and E. Aharonov (1998), Periodic formation of magma fractures and generation of layered gabbros in the lower crust beneath oceanic spreading ridges, in *Faulting and Magmatism at Mid-Ocean Ridges, Geophys. Monogr. Ser.*, 106, edited by W. R. Buck et al., pp. 267–289, AGU, Washington, D. C., doi:10.1029/GM106p0267.

Kelemen, P. B., H. J. B. Dick, and J. E. Quick (1992), Formation of harzburgite by pervasive melt/rock reaction in the upper mantle, *Nature*, *358*, 635–641, doi:10.1038/358635a0.

Kelemen, P. B., N. Shimizu, and V. J. Salters (1995), Extraction of mid-ocean-ridge basalt from the upwelling mantle by focused flow of melt in dunite channels, *Nature*, *375*, 747–753, doi:10.1038/375747a0.

Key, K., S. Constable, L. Liu, and A. Pommier (2013), Electrical image of passive mantle upwelling beneath the northern East Pacific Rise, *Nature*, *495*, 499–502, doi:10.1038/nature11932.

Kinzler, R. J. (1997), Melting of mantle peridotite at pressures approaching the spinel to garnet transition: Application to mid-ocean ridge basalt petrogenesis, *J. Geophys. Res.*, *102*, 853–874, doi:10.1029/96JB00988.

Kinzler, R. J., and T. L. Grove (1992), Primary magmas of mid-ocean ridge basalts 1. Experiments and methods, *J. Geophys. Res.*, *97*, 6885–6906, doi:10.1029/91JB02840.

Klein, E. M., and C. H. Langmuir (1987), Global correlations of ocean ridge basalt chemistry with axial depth and crustal thickness, *J. Geophys. Res.*, *92*, 8089–8115, doi:10.1029/JB092iB08p08089.

Korenaga, J., and P. B. Kelemen (1997), Origin of gabbro sills in the Moho transition zone of the Oman ophiolite: Implications for magma transport in the oceanic lower crust, *J. Geophys. Res.*, *102*, 27,729–27,749, doi:10.1029/97JB02604.

Kuo, B. Y., and D. Y. Forsyth (1988), Gravity anomalies of the ridge-transform system in the South Atlantic between 31 and 34.5°S: Upwelling centers and variations in crustal thickness, *Mar. Geophys. Res.*, *10*, 205–232, doi:10.1007/BF00310065.

Langmuir, C. H., E. M. Klein, and T. Plank (1992), Petrological systematics of mid-ocean ridge basalts: Constraints on melt generation beneath ocean ridges, in *Mantle Flow and Melt Generation at Mid-Ocean Ridges, Geophys. Monogr. Ser.*, 71, edited by J. Phipps Morgan, D. K. Blackman, and J. M. Sinton, pp. 183–280, AGU, Washington, D. C.

Le Pichon, X., R. E. Houtz, C. L. Drake, and J. E. Nafe (1965), Crustal structure of the mid-ocean ridges: 1. Seismic refraction measurements, *J. Geophys. Res.*, *70*, 319–339, doi:10.1029/JZ070i002p00319.

Lin, J., and J. Phipps Morgan (1992), The spreading rate dependence of three-dimensional mid-ocean ridge gravity structure, *Geophys. Res. Lett.*, *19*, 13–16, doi:10.1029/91GL03041.

Lin, J., G. M. Purdy, H. Schouten, J. C. Sempere, and C. Zervas (1990), Evidence from gravity data for focused magmatic accretion along the Mid-Atlantic Ridge, *Nature*, *344*, 627–632, doi:10.1038/344627a0.

Macdonald, K. C. (1982), Mid-ocean ridges: Fine scale tectonic, volcanic and hydrothermal processes within the plate boundary zone, *Annu. Rev. Earth Planet. Sci.*, *10*, 155–190, doi:10.1146/annurev.ea.10.050182.001103.

Macdonald, K. C., P. J. Fox, R. T. Alexander, R. Pockalny, and P. Gente (1996), Volcanic growth faults and the origin of Pacific abyssal hills, *Nature*, *380*, 125–129, doi:10.1038/380125a0.

Magde, L. S., and D. W. Sparks (1997), Three-dimensional mantle upwelling, melt generation, and melt migration beneath segment slow spreading ridges, *J. Geophys. Res.*, *102*, 20,571–20,583, doi:10.1029/97JB01278.

McKenzie, D. P. (1985), ^{230}Th-^{238}U disequilibrium and the melting processes beneath ridge axes, *Earth Planet. Sci. Lett.*, *72*, 149–157, doi:10.1016/0012-821X(85)90001-9.

McKenzie, D., and M. J. Bickle (1988), The volume and composition of melt generated by extension of the lithosphere, *J. Petrol.*, *29*, 625–679, doi:10.1093/petrology/25.3.713.

MELT Seismic Team (1998), Imaging the deep seismic structure beneath a mid-ocean ridge: The MELT experiment, *Science*, *280*, 1215–1218, doi:10.1126/science.280.5367.1215.

Miller, K. J., L. G. J. Montési, and W. Zhu (2014), Experimental quantification of permeability for partially molten mantle rocks, *Earth Planet. Sci. Lett.*, *432*, 332–341, doi:10.1016/j.epsl.2015.10.004.

Montési, L. G. J., and M. D. Behn (2007), Mantle flow and melting underneath oblique and ultraslow mid-ocean ridges, *Geophys. Res. Lett.*, *34*, L24307, doi:10.1029/2007GL031067.

Montési, L. G. J., M. D. Behn, L. B. Hebert, J. Lin, and J. L. Barry (2011), Controls on melt migration and extraction at the ultraslow Southwest Indian Ridge 10–16°E, *J. Geophys. Res.*, *116*, B10102, doi:10.1029/2011JB008259.

Nicolas, A. (1986), A melt extraction model based on structural studies in mantle peridotites, *J. Petrol.*, *27*, 999–1022, doi:10.1093/petrology/27.4.999.

Nicolas, A. (1990), Melt extraction from mantle peridotites: Hydrofracturing and porous flow, with consequences for oceanic ridge activity, in *Magma Transport and Storage*, edited by M. P. Ryan, pp. 159–174, Wiley, New York.

Nicolas, A., F. Boudier, and B. Ildefonse (1996), Variable crustal thickness in the Oman ophiolite: Implication for oceanic crust, *J. Geophys. Res.*, *101*, 17–941, doi:10.1029/96JB00195.

O'Haver, T. (2008), Fast smoothing function, in *MATLAB Central*, MathWorks, Natick, Mass. [Available at https://www.mathworks.com/matlabcentral/fileexchange/19998-fast-smoothing-function.]

Perfit, M. R., et al. (1996), Recent volcanism in the Siqueiros transform fault: Picritic basalts and implications for MORB magma genesis, *Earth Planet. Sci. Lett.*, *141*, 91–108, doi:10.1016/0012-821X(96)00052-0.

Reid, I., and H. R. Jackson (1981), Oceanic spreading rate and crustal thickness, *Mar. Geophys. Res.*, *5*, 165–172, doi:10.1007/BF00163477.

Sinton, J., E. Bergmanis, K. Rubin, R. Batiza, T. K. P. Gregg, K. Grönvold, K. C. Macdonald, and S. M. White (2002), Volcanic eruptions on mid-ocean ridges: New evidence from the superfast spreading East Pacific Rise, 17°–19°S, *J. Geophys. Res.*, *107*(B6), doi:10.1029/2000JB000090.

Sleep, N. H. (1988), Tapping of melt by veins and dikes, *J. Geophy. Res.*, *93*, 10,255–10,272, doi:10.1029/JB093iB09p10255.

Smith, D. K., and J. R. Cann (1999), Constructing the upper crust of the Mid-Atlantic Ridge: A reinterpretation based on the Puna Ridge, Kilauea Volcano, *J. Geophys. Res.*, *104*, 25,379–25,399, doi:10.1029/1999JB900177.

Smith, P. M., and P. D. Asimow (2005), Adiabat_1ph: A new public front-end to the MELTS, pMELTS, and pHMELTS models, *Geochem. Geophys. Geosyst.*, *6*, Q02004, doi:10.1029/2004GC000816.

Sparks, D. W., and E. M. Parmentier (1991), Melt extraction from the mantle beneath spreading centers, *Earth Planet. Sci. Lett.*, *105*, 368–377, doi:10.1016/0012-821X(91)90178-K.

Spiegelman, M., and D. McKenzie (1987), Simple 2-D models for melt extraction at mid-ocean ridges and island arcs, *Earth Planet. Sci. Lett.*, *83*, 137–152, doi:10.1016/0012-821X(87)90057-4.

Till, C. B., T. L. Grove, and M. J. Krawczynski (2012), A melting model for variably depleted and enriched lherzolite in the plagioclase and spinel stability fields, *J. Geophys. Res.*, *117*, B06206, doi:10.1029/2011JB009044.

White, R. S. (1997), Rift-plume interaction in the North Atlantic, *Philos. Trans. R. Soc. London A*, *355*, 319–339, doi:10.1098/rsta.1997.0011.

White, R. S., T. A. Minshull, M. J. Bickle, and C. J. Robinson (2001), Melt generation at very slow-spreading oceanic ridges: Constraints from geochemical and geophysical data, *J. Petrol.*, *42*(6), 1171–1196, doi:10.1093/petrology/42.6.1171.

Wilson, C. R., M. Spiegelman, P. E. van Keken, and B. R. Hacker (2014), Fluid flow in subduction zones: The role of solid rheology and compaction pressure, *Earth Planet. Sci. Lett.*, *401*, 261–274, doi:10.1016/j.epsl.2014.05.052.

Workman, R. K., and S. R. Hart (2005), Major and trace element composition of the depleted MORB mantle (DMM), *Earth Planet. Sci. Lett.*, *231*, 53–72, doi:10.1016/j.epsl.2004.12.005.

Yang, H. J., R. J. Kinzler, and T. L. Grove (1996), Experiments and models of anhydrous, basaltic olivine-plagioclase-augite saturated melts from 0.001 to 10 kbar, *Contrib. Mineral. Petrol.*, *124*, 1–18, doi:10.1007/s004100050169.